Applied Physics Letters

RESEARCH ARTICLE | JULY 30 2025

Nm-scale electrical resistance imaging on CdTe by scanning spreading resistance microscopy

C.-S. Jiang ; H. Lott ; A. T. Mathew ; M. Nardone ; E. Colegrove ; M. O. Reese

Appl. Phys. Lett. 127, 043904 (2025)
https://doi.org/10.1063/5.0268718

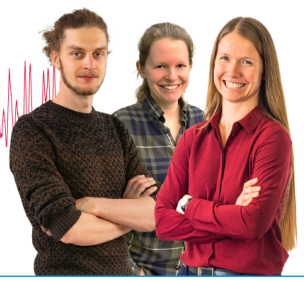

Applied Physics Letters ARTICLE pubs.aip.org/aip/apl

Nm-scale electrical resistance imaging on CdTe by scanning spreading resistance microscopy

Cite as: Appl. Phys. Lett. **127**, 043904 (2025); doi: 10.1063/5.0268718
Submitted: 3 March 2025 · Accepted: 9 July 2025 ·
Published Online: 30 July 2025

C.-S. Jiang,[1,a] H. Lott,[1] A. T. Mathew,[1,2] M. Nardone,[3] E. Colegrove,[1] and M. O. Reese[1]

AFFILIATIONS

[1]National Renewable Energy Laboratory, Golden, Colorado 80401, USA
[2]Colorado School of Mines, Golden, Colorado 80401, USA
[3]Bowling Green State University, Bowling Green, Ohio 43403, USA

[a]Author to whom correspondence should be addressed: chun.sheng.jiang@nrel.gov

ABSTRACT

Local resistance imaging can provide information on nm-scale carrier distribution in semiconductor devices. Scanning spreading resistance microscopy (SSRM), an atomic force microscopy-based nm-scale resistance mapping technique, has been developed for carrier delineation in Si microdevices. We report on the development and validation of SSRM on CdTe materials, by testing on molecular beam epitaxy (MBE) grown CdTe films. The probe/CdTe contact resistance was suppressed sufficiently below sample's spreading resistance by pressing the probe into the sample with ∼mN contact force and applying a large sample/probe forward bias voltage (V_s), which was understood by analyzing current-voltage (I-V) involving a serially connected insulating top layer with underlying spreading resistance. The carrier concentration as deduced from the resistance measurement, using a single mobility value, is consistent with Hall measurement with a standard deviation of 14% based on a set of MBE films with carrier concentrations in the range of 10^{15}–10^{16}/cm^3. The doping polarity was readily identified by flipping V_s polarity, where the resistance with reverse V_s is orders of magnitude larger than forward V_s. While focusing on the SSRM technique validation, we also show an example on an As-doped Cd(Se,Te) polycrystalline thin film of a high-performance CdTe solar cell, which illustrates the local resistance nonuniformity with up to two orders of magnitude differences, indicating if local mobility is roughly constant, local carrier concentration can have significant nonuniformity.

Nanometer resolution resistance measurement, which images the doping nonuniformity that could be detrimental for device performance, is a highly demanded characterization technique in thin film photovoltaic (PV) technologies. A recent focus in CdTe PV research is group-V (Gr-V) doping. This has effectively increased the doping limit of traditional Cu-doping from ∼10^{14} to ∼10^{16} cm^{-3} and has enabled open circuit voltage V_{oc} ∼ 920 mV in high-performance polycrystalline Cd(Se,Te) devices with a bandgap (Eg) of ∼1.4 eV. This high V_{oc} for Cd(Se,Te) devices matches the bandgap equivalent V_{oc} realized in single crystalline CdTe (Eg ∼ 1.5 eV) model devices nearly a decade ago[1–6] but is still 200 mV below the detailed balance limit for the respective band gaps (1.4 eV → 1122 mV; 1.5 eV → 1215 mV).[7] Both group-V dopants and Se alloying can significantly alter the defect chemistry in polycrystalline PV devices[8–12] and introduce nonuniformities in doping, minority carrier lifetime, and front and back interface recombination. On the other hand, device design that introduces specific local doping profiles can be a route to improve the device performance. For example, heavy doping on back side of CdTe absorber may improve V_{oc} by lowering the potential barrier at the back contact. Resistance imaging with nm-resolution in both lateral and vertical directions can meet these doping-related device characterization needs.

Scanning spreading resistance microscopy (SSRM) is an atomic force microscopy (AFM)-based electrical probe that maps the resistance distribution of semiconductors with nm-resolution.[13–15] SSRM has been developed mainly for micro-Si devices. Instead of mapping extrinsic doping elements, SSRM directly maps the active charge carrier distributions. The measured resistance R_{tot} [Figs. 1(a) and 1(b)] is the sum of series resistance along the current path from the probe to the back contact. The back-contact resistance R_b (10^2–10^3 Ω) is very small compared to the other resistance contributors due to the large contact area, allowing it to be neglected. The probe/sample contact resistance R_c can be minimized to a degree much smaller than the sample's spreading resistance (R_{sp}), by pressing the probe hard into

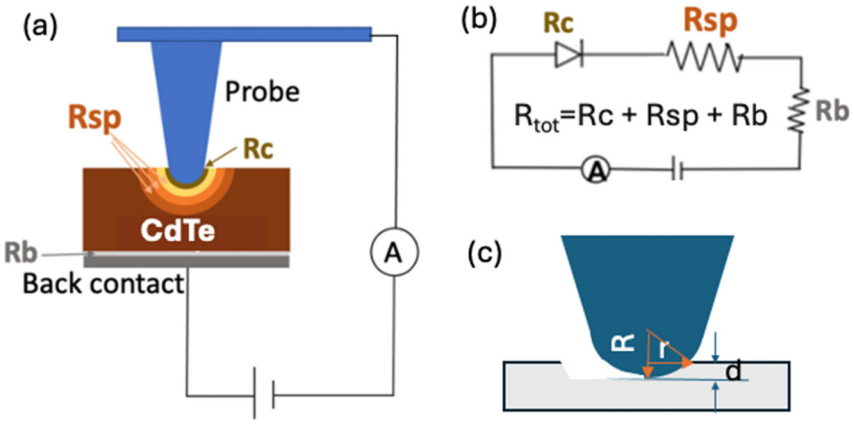

FIG. 1. Schematics of (a) SSRM set-up, (b) equivalent electrical circuit, and (c) probe/sample contacts. R_{tot}, R_c, R_{sp}, and R_b denote the measured, probe/sample contact, sample's spreading, and sample/back-contact resistances, respectively. R, r, and d are probe radius, probe/sample contact radius, and probe scratch depth into the sample, respectively.

sample to create a local region of strained and dangling bonds around the probe/sample contact and by applying a large forward bias voltage to the sample/probe contact diode.[13,14] Therefore, the measured R_{tot} is dominated by sample's spreading resistance, R_{sp}. R_{sp} is further dominated by the resistance of nm-size volume right beneath the probe, as the resistance decays rapidly with distance away from the probe. This scheme enables nm-resolution resistance mapping by SSRM. SSRM provides local resistivity mapping by $\rho = 4rR_{sp}$, where ρ is the local resistivity and r and R_{sp} are the probe/sample contact radius and spreading resistance, respectively.

In this contribution, we report on the development and validation of SSRM for CdTe materials. We have previously reported the resistance imaging on CdSeTe thin films for PV[16] using SSRM, which showed nonuniform resistance distributions. Application of SSRM on CdTe materials must be validated to demonstrate that the nm-scale resistance mapping technique can be applied to CdTe materials, which is the focus here. We have validated the technique on molecular beam epitaxial (MBE) grown single crystalline CdTe thin films with well-controlled carrier concentration and mobility. While focusing on the SSRM technique, an example of its application in As-doped Cd(Se,Te) polycrystalline films for high-performance CdTe solar cells is also given.

The AFM (Bruker Dimension Icon and Nanoscope V controller) is set up in an Ar glovebox. SSRM (Bruker SSRM module) has a logarithm-scale current amplifier with a wide range of resistance measurement (10^3–10^{14} Ω). Sample/probe bias voltage (V_s) is applied to the sample, and the probe is floating-grounded to keep the probe potential at the ground level, with all the current flowing through the probe conducted to the amplifier. A diamond-coated Si probe (Bruker DDESP-V2) is pressed into the sample material during scanning with a large contact force of ∼1 mN. The diamond coating is highly B-doped (∼10^{-4} Ωcm) and can be approximated as metallic. The current-voltage (I-V) is measured by taking the average of resistance images with a fixed V_s, rather than running I-V sweeps at fixed location. This approach ensures the measurement accuracy because the bandwidth of the amplifier is narrow at small currents, and the fixed probe/sample contact is not adequately stable for sweeping V_s in seconds.

The MBE films were grown in a Veeco Gen930 system on 3″ Si ⟨211⟩ substrates. Undoped layers of CdTe were initially deposited to a thickness of 5 μm,[17] followed by 3 μm thick As-doped layers with a target As incorporation level of 10^{17} cm^{-3} doping.[18] The samples were then annealed in a rapid thermal processing tool (400–600 °C) for 10 min. Au contacts were applied to 1 × 1 cm pieces for standard Van der Pauw Hall measurements. For n-type films, indium doping and contacts were used. Different annealing and growth conditions result in samples with different carrier concentrations and mobilities, which were analyzed by SRRM in this work.

Figure 2 shows resistance images taken under forward and reverse biases on a p-type MBE film with Hall carrier concentration $C_H = 3.5 \times 10^{16}/cm^3$. The resistance with $V_s = +10$ V [Fig. 2(a)] is homogeneous across the image, with an average value $R = 4.72 \times 10^5$ Ω and a relative standard deviation Rq/R = 0.11, where $Rq = 5.39 \times 10^4$ Ω is the standard deviation of the resistance. The small variation is likely induced by surface corrugation as observed in the corresponding AFM image [Figs. 2(g) and 2(h)] due to dislocation cores formed during MBE growth. The resistance map with $V_s = -10$ V [Fig. 2(c)] shows an average value of three orders of magnitude larger than that at $V_s = +10$ V, and the resistance is inhomogeneous with variation of several orders of magnitude [Fig. 2(d)]. An image with both V_s polarities is also shown in Fig. 2(e). While the resistance with forward V_s for the p-type CdTe is dominated by the spreading resistance R_{sp}, as will be discussed later, the resistance under a negative V_s is dominated by contact resistance R_c, which is not stable during the imaging.

Figure 3 shows a resistance-voltage (R-V_s) plot [Fig. 3(a)] and converted I-V plot [Fig. 3(b)] at positive V_s on an MBE film with $C_H = 8.5 \times 10^{15}/cm^3$. Each resistance data point in Fig. 3(a) was averaged over four individual SSRM images. I-V modeling analysis [curve in Fig. 3(b)] suggests that the contact resistance, R_c, in forward V_s is compatible with charge transport through an insulating layer,[19,20] instead of a Schottky contact. The voltage drop ($V_s = V_{in} + V_{sc} + V_{sp}$) should be the result of insulator top layer (if any), Schottky contact, and the sample's spreading resistance in series. I-V fitting suggests that V_{in} dominates the voltage drop in low V_s, while V_{sp} dominates in high V_s regions. V_{sc} makes a minor contribution in low V_s region. The I-V analysis [curve in Fig. 3(b)] fits with $V = V_{in} + V_{sp}$ by neglecting V_{sc} or approximating flatband beneath the insulating layer, since the conductance in the Schottky contact is largely enhanced by a small V_{sc} when forward V_s is applied. However, this forward V_s-induced conduction does not apply to reverse V_s; a large reverse V_{sc} can drop on

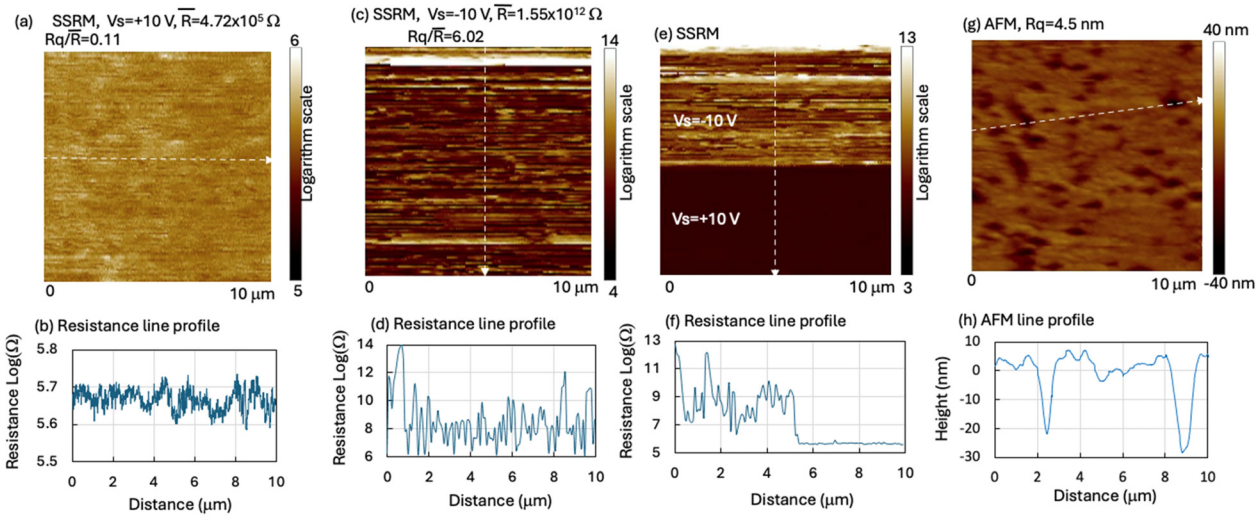

FIG. 2. SSRM resistance images taken on a p-type MBE film with (a) Vs=+10 V, (c) Vs = −10 V, and (e) both polarities. (g) The AFM image simultaneously taken with (a). (b), (d), (f), and (h) are example line profiles along the lines in the corresponding images.

the Schottky contact. For I-V across the insulating layer, we used Poole-Frenkel's approach for charge transport,[19,20] where charges hop between trapping centers by electric field. I-V of this approach can be described as

$$I = ACE\exp\left[-\frac{q(\phi - aE^{1/2})}{kT}\right], \quad \text{where } a = \sqrt{q/\pi\varepsilon_0\varepsilon_{in}},$$

where E is the electric field across the oxide, ϕ is the barrier height of charge trapping center, A is the probe/sample contact area, C depends on the density of charge trapping centers, q is the elemental charge, k is the Boltzmann constant, T is the temperature, ε_0 is the permittivity of free space, and ε_{in} is the insulator dielectric constant. The I-V fitting input parameters include charge excitation barrier of $\phi = 0.52$ V and probe/sample contact radius 50 nm. The parameters of insulator dielectric constant ε_{in} and insulator thickness (Th) are inter-dependent, with corresponding $\varepsilon_{in} = 10$–3 and Th = 7.5–25 nm, all in reasonable ranges. We used $R_{sp} = 1.0 \times 10^6$ Ω, a slightly larger value than measured by SSRM to account the small contact resistance R_c in the high Vs range. Reasonable agreement between the transport model and the I-V data is shown in Fig. 3(b). The model parameter values serve as rough estimates but suffice to indicate that a defect-mediated transport mechanism with exponential field dependence likely dominates in the low voltage regime followed by linear bias dependence due to the Ohmic spreading resistance at higher voltages. We note that if such I-V measurements were conducted on the bare back surface of PV film without device back contact, contact would be made between the device front contact transparent condictive oxide (TCO) and SSRM probe/film point contact (nm-scale sizes), and the current path would spread from the point contact to TCO, which is different from the device dark I-V measurement. Furthermore, if the probe contact was made on the device conductive back contact, the SSRM fine resolution would be lost.

Table I lists MBE-samples used in the SSRM test. The left three samples have well-defined Hall carrier concentration, C_H, and similar Hall mobility μ_H. To reduce fitting parameters, we assume the same mobility and fit inverse resistance (1/R) vs C_H [blue circle symbols in Fig. 4(a)] by $C_H = 1/\rho\mu q = (1/4qr_{eff}\mu) \times (1/R)$, where $\rho = 4r_{eff}R$ is the local resistivity of the sample, r_{eff} is the effective probe/sample contact radius, and μ is the charge mobility. Data in column 4 were not included in the fitting because C_H was below 10^{15}/cm^3 (orange square symbol), and this C_H is too low for our Hall set-up to measure reliably. The linear fitting yields $\mu \times r_{eff} = (1.05 \pm 0.11) \times 10^{-4}$ cm^3/V$_s$.

Despite the probe radius of R∼100 nm, the actual contact radius can be significantly off as only the probe apex contacts the sample, and it depends on probe/sample contact force. We further measured r_{eff} by imaging scratch depth before and after SSRM, using the contact AFM mode with a very gentle contact force that does not scratch sample materials off (Fig. 5). The scratch image was obtained by subtracting the AFM image before SSRM [Fig. 5(b)] from the image after SSRM [Fig. 5(a)]. The scratch depth [Fig. 5(d)] was obtained by averaging line profiles in the SSRM-scratched area [Fig. 5(c)]. From the scratch depth d and probe radius R, the contact radius r was deduced [Fig. 1(c)]. Because only the front half of the probe apex contacts the sample as it digs into the sample and scans linearly, the effective radius is $r_{eff} = r/\sqrt{2}$. From the fitting product $\mu \times r_{eff}$, mobility μ_s of each sample is estimated and listed in Table I, which is about consistent with the Hall mobility μ_H. Carrier concentration C_S is further deduced from the SSRM resistance R, r_{eff}, and μ_s, which is consistent with Hall measurement C_H [Fig. 4(b) and Table I]. For the sample with $C_H = 1 \times 10^{14}$–1×10^{15}/cm^3, SSRM measures $C_S = 1.13 \times 10^{15}$/cm^3 when using the fitting mobility from the other three samples. Therefore, SSRM measures the spreading resistance R_{sp} quantitatively despite the presence of a top insulating layer. The converted C_S is consistent with Hall measurement C_H with a standard deviation of 14% for these MBE films. Relative carrier concentration can be deduced if a set of samples or different locations in a sample with similar mobilities are measured. There is some evidence that this is the situation for polycrystalline CdTe films, where carrier concentration varies but mobility remains

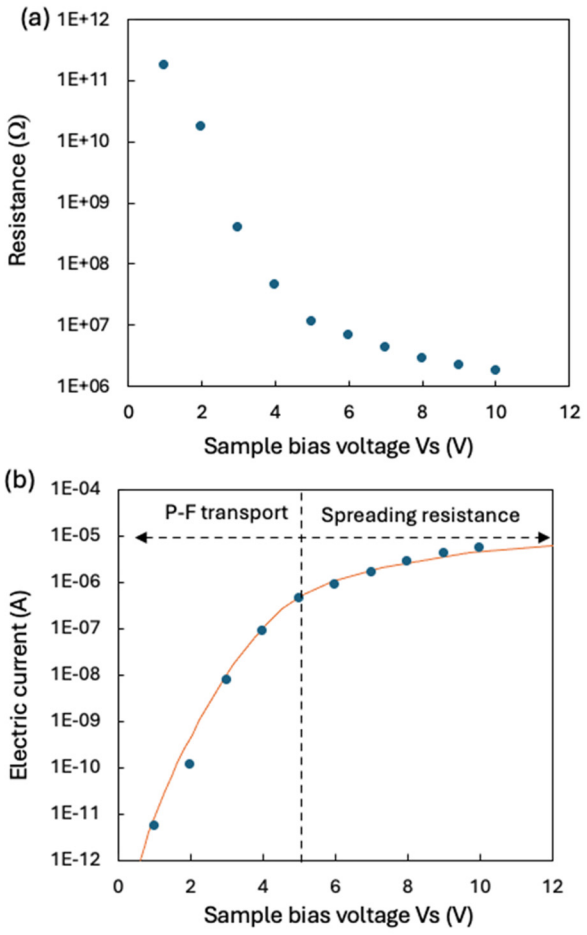

FIG. 3. Graphs of (a) resistance vs V_s and (b) converted I-V. The I-V curve in (b) is an analysis described in the text. The curve represents the transport model with combined Poole-Frenkel and spreading resistance compared to the data (points) with the vertical dashed line delineating the two regions—the dominating V_s of the spreading resistance and the transport over insulating layer.

comparatively constant.[21] Mobility in polycrystalline CdTe and Cd(Se,Te) has not been measured as frequently as carrier concentration; however, some of the measurements that have been done indicate that the polycrystalline films may have several orders of magnitude lower mobility compared to single crystals.[21,22] Detailed mobility analysis is outside the scope of this work, but we plan to incorporate any new data as they become available in future analysis.

We also tested SSRM on an n-type In-doped MBE sample (Fig. 6). The resistance [Figs. 6(a) and 6(b)] is very uniform and low due to the larger electron mobility than holes (right column in Table I). The resistance with positive V_s [Figs. 6(c) and 6(d)] is many orders of magnitude larger than that with negative V_s, opposite to the p-type MBE samples above, demonstrating the n-type doping. An image with changing V_s polarity [Figs. 6(e) and 6(f)] illustrates the large difference in the resistance values. Therefore, doping type with decent carrier concentrations is readily identified by flipping the V_s polarity. The C_s value is approximately consistent with Hall measurement C_H, with a difference of 21% when using the Hall mobility μ_H value. Resistance measured under positive V_s is several orders of magnitude larger than negative V_s, consistent with the polarity of Schottky contact. Therefore, doping type can be identified by flipping the V_s polarity. The small relative standard deviation Rq/R = 0.63 [Fig. 6(a)] is caused by the surface effect, where the SSRM image [Fig. 6(a)] correlates closely with the AFM image [Fig. 6(g)]. However, this small resistance fluctuation does not significantly affect the data quality.

Finally, we show an example of SSRM application on a typical polycrystalline Cd(Se,Te) film during high-performance PV R&D (Fig. 7); two more SSRM images taken in randomly selected areas on the same sample are shown in the supplementary material (Fig. S1). The SSRM was taken on the back surface of the As-doped Cd(Se,Te) film deposited on a SnO_2 TCO-coated glass superstrate. The resistance distribution is nonuniform with high resistance regions two orders of magnitude higher than the most areas [Fig. 7(b)]. From the average resistance $R = 4.8 \times 10^6\ \Omega$ (averaged after removing the distinct high resistance regions as the high resistance would dominate the average value if they were included), the average carrier concentration is $C_S = 1.7 \times 10^{16}/\text{cm}^3$, assuming hole mobility $\mu = 10\ \text{cm}^2/\text{V s}$[21] and effective contact radius $r_{eff} = 22$ nm (the same as the MBE films), consistent with C-V measurement on similar devices ($\sim 1 \times 10^{16}/\text{cm}^3$).

TABLE I. A summary of Hall and SSRM measurements on five MBE-samples. Left 3 columns are the three p-type films with similar Hall mobilities that were used in the linear fitting. The left 4th column is a p-type film with low uncertain Hall carrier concentration and Hall mobility. The right column is a n-type film. MBE sample IDs relate to 1 cm × 1 cm sub-pieces of larger 3-inch wafers.

MBE samples	RC4 p-type	LC5 p-type	LC6 p-type	LL2 p-type	LL3 n-type
Hall carrier concentration C_H (cm^{-3})	3.5×10^{16}	1.91×10^{16}	8.3×10^{15}	1×10^{14}–1×10^{15}	3.3×10^{16}
Hall mobility μ_H (cm^2/V_s)	63	76	76	N.A.	731
Measured resistance R (Ω)	4.58×10^5	6.80×10^5	1.48×10^6	1.31×10^7	2.60×10^4
SSRM carrier concentration C_s (cm^{-3})	3.24×10^{16}	2.18×10^{16}	1.00×10^{16}	1.13×10^{15}	2.6×10^{16}
Scratch depth/effective contact radius, r_{eff} (nm)	5 nm/22 nm	5 nm/22 nm	4 nm/19.8 nm	5 nm/22 nm	10 nm/31 nm
SSRM mobility μ_s (cm^2/V_s)	48	48	53	48	731 (μ_H)

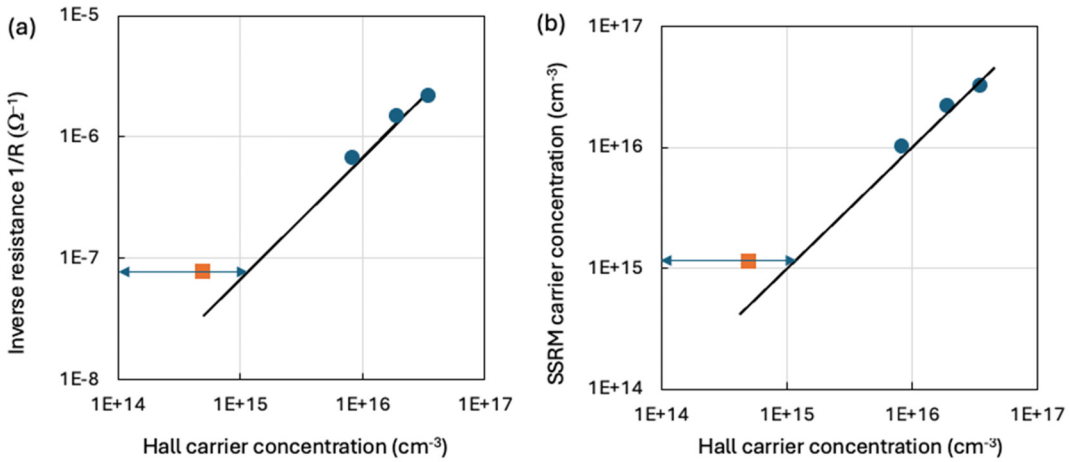

FIG. 4. (a) Linear fitting of inverse resistance (1/R) with Hall carrier concentration C_H and (b) SSRM C_S vs C_H.

We note that these parameter assumptions have not been verified particularly on the film investigated, and the values may be off. While mobility of the MBE single crystalline films was deduced from fitting the inverse resistance to Hall carrier concentrations, the mobility in the polycrystalline films cannot be directly quantified since it may vary along with the carrier concentration and selenium concentration. The resistance fluctuates moderately in a factor of 2–3 times in majority regions of the film [Fig. 7(c)]. In addition, there are regions in sizes of sub-μm to a few μm with distinctly high resistance of up to two orders of magnitude variation [Fig. 7(b)], possibly resulting from local stoichiometry and structure differences. Grain structure and grain boundary (GB) are visible from both the resistance and AFM surface topographic maps. The resistance on the GBs is slightly lower than the grain interior (a fraction of the resistance) with widths of 100–200 nm [dashed oval in Fig. 7(c)]. Rather, the resistance among the grains and regions inside grains fluctuates more in a factor of 2–3 times. These resistance features were observed on the back surface of the film and can change with depth into the film bulk,[16] which will be investigated in the future by bevel-polishing into the film bulk. The resistance nonuniformity suggests similar carrier concentration nonuniformity, assuming the carrier concentration varies more than mobility. Crystalline orientation-dependent mobility[23] may affect the resistance nonuniformity between grains. Given that related to high-performance devices, the resistance fluctuation being present on these devices suggests that it is not inherently limiting the current high efficiency ranges, but it may still be limiting future performance improvement. We note that the consistently observed large resistance nonuniformity on the back surface of the high-performance films was confirmed not to be an artifact of surface morphology or contamination, as the resistance images do not correlate well to the surface morphology. However, the resistance variation on grain boundaries cannot be excluded from the surface effect, as the resistance variation is small, and the surface height changes are pronounced at the GBs. On the other hand, the lower resistance on GBs can be an explanation for the larger GB signal of electron beam-induced current along with other explanations such as field-collection.[24–26] The example here demonstrates the value of SSRM as applied to CdTe thin film PV.[16]

In conclusion, we have validated the SSRM imaging on CdTe materials by testing on well-controlled MBE films with known Hall carrier concentration and mobility. The results demonstrate quantitative measurement with 14% standard deviation from Hall measurement, giving confidence in probe contact area and a plausible upper bound of local mobility in p-type CdTe. Doping types with carrier concentration in $\sim 10^{15}/cm^3$ or larger can be readily identified by flipping probe/sample bias voltage polarities. The probe/CdTe contact resistance was minimized by pressing the probe into the film and applying

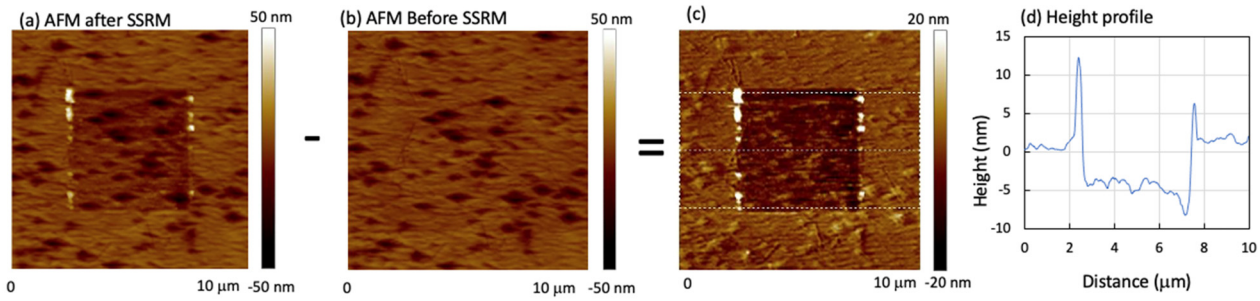

FIG. 5. AFM images taken (a) after and (b) before a SSRM imaging and (c) their difference. (d) The profile averaged from the scratched area in (c).

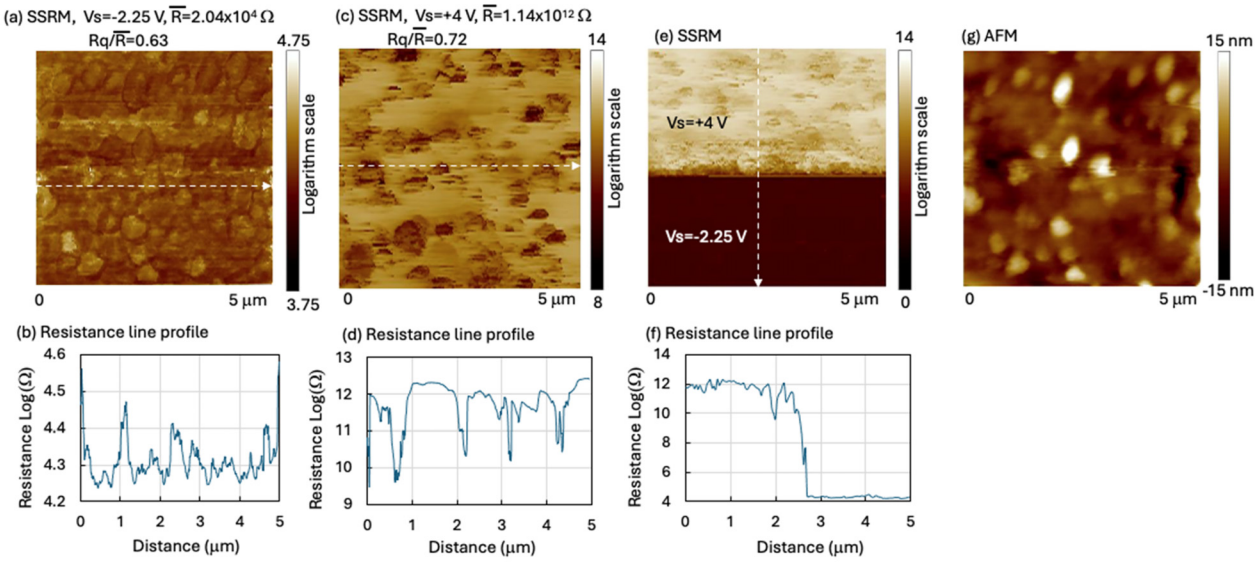

FIG. 6. SSRM resistance images taken on an n-type MBE film with (a) $V_s = -2.25$ V, (c) $V_s = +4$ V, and (e) both polarities. (g) The AFM image simultaneously taken with (a). (b), (d), and (f) Example line profiles along the lines in the corresponding images.

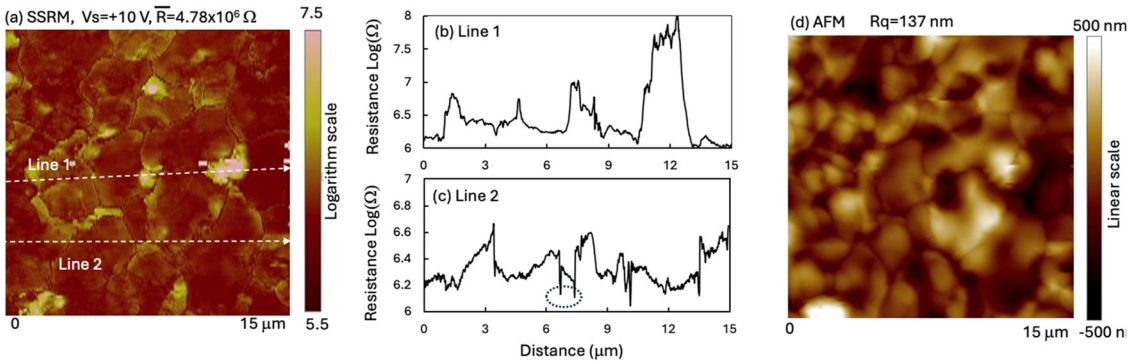

FIG. 7. (a) An SSRM resistance image taken on the back surface of an As-doped Cd(Se,Te) polycrystalline thin film. (b) and (c) Two example resistance line profiles along the lines in (a). (d) The AFM images taken simultaneously with (a).

a large probe/film forward bias voltage, so that the measured resistance is dominated by sample's spreading resistance in high voltage range ($V_s > 5$ V). The I-V analysis suggests that defect-mediated transport through a thin insulator or defective region could dominate the resistance in the low V_s range ($V_s < 5$V). An example of the SSRM application in current CdTe PV R&D efforts is given on an As-doped Cd(Se,Te) polycrystalline thin film. The results illustrate the large resistance fluctuation up to two orders of magnitudes at the back surface of the film. SSRM is expected to apply widely in CdTe-based materials and devices beyond PV technology.

See the supplementary material for SSRM resistance images taken in more areas of the polycrystalline Cd(Se,Te) film to show representative resistance features observed.

This work was authored by the National Renewable Energy Laboratory, operated by Alliance for Sustainable Energy, LLC, for the U.S. Department of Energy (DOE) (Contract No. DE-AC36-08GO28308). Funding provided by the U.S. Department of Energy's Office of Energy Efficiency and Renewable Energy (EERE) Solar Energy Technologies Office (SETO) Agreement with agreement number 38257. The views expressed in the article do not necessarily represent the views of the DOE or the U.S. Government. The U.S. Government retains and the publisher, by accepting the article for publication, acknowledges that the U.S. Government retains a nonexclusive, paid-up, irrevocable, worldwide license to publish or reproduce the published form of this work, or allow others to do so, for U.S. Government purposes.

AUTHOR DECLARATIONS

Conflict of Interest

The authors have no conflicts to disclose.

Author Contributions

C.-S. Jiang: Conceptualization (equal); Data curation (equal); Formal analysis (equal); Investigation (equal); Methodology (equal); Writing – original draft (equal). **H. Lott:** Data curation (equal); Formal analysis (equal); Investigation (equal); Methodology (equal); Writing – review & editing (equal). **A. T. Mathew:** Data curation (equal); Formal analysis (equal); Investigation (equal); Methodology (equal); Writing – review & editing (equal). **M. Nardone:** Conceptualization (equal); Data curation (equal); Formal analysis (equal); Investigation (equal); Methodology (equal); Writing – review & editing (equal). **E. Colegrove:** Conceptualization (equal); Formal analysis (equal); Investigation (equal); Methodology (equal); Supervision (equal); Writing – review & editing (equal). **M. O. Reese:** Conceptualization (equal); Formal analysis (equal); Funding acquisition (equal); Investigation (equal); Methodology (equal); Supervision (equal); Writing – review & editing (equal).

DATA AVAILABILITY

The data that support the findings of this study are available from the corresponding author upon reasonable request.

REFERENCES

[1]R. Mallick, X. Li, C. Reich, X. Shan, W. Zhang, T. Nagle, L. Bok, E. Bicakci, N. Rosenblatt, D. Modi, R. Farshchi, C. Lee, J. Hack, S. Grover, N. Wolf, W. K. Metzger, D. Lu, and G. Xiong, "Arsenic-doped CdSeTe solar cells achieve world record 22.3% efficiency," IEEE J. Photovoltaics **13**(4), 510–515 (2023).

[2]W. K. Metzger, S. Grover, D. Lu, E. Colegrove, J. Moseley, C. L. Perkins, X. Li, R. Mallick, W. Zhang, R. Malik, J. Kephart, C.-S. Jiang, D. Kuciauskas, D. S. Albin, M. M. Al-Jassim, G. Xiong, and M. Gloeckler, "Exceeding 20% efficiency with in situ group V doping in polycrystalline CdTe solar cells," Nat. Energy **4**(10), 837–845 (2019).

[3]W. K. Metzger, D. W. Miller, R. Mallick, X. Li, W. Zhang, I. Wang, A. Polizzotti, T. Ablekim, D. H. Cao, D. C. Hamilton, J. Bailey, C. Lee, S. Grover, D. Lu, and G. Xiong, "As-doped CdSeTe solar cells achieving 22% efficiency with −0.23%/°C temperature coefficient," IEEE J. Photovoltaics **12**(6), 1435–1438 (2022).

[4]J. M. Burst, J. N. Duenow, D. S. Albin, E. Colegrove, M. O. Reese, J. A. Aguiar, C.-S. Jiang, M. K. Patel, M. M. Al-Jassim, D. Kuciauskas, S. Swain, T. Ablekim, K. G. Lynn, and W. K. Metzger, "CdTe solar cells with open-circuit voltage breaking the 1 V barrier," Nat. Energy **1**(3), 1–8 (2016).

[5]J. M. Burst, J. N. Duenow, A. Kanevce, H. R. Moutinho, C. S. Jiang, M. M. Al-Jassim, M. O. Reese, D. S. Albin, J. A. Aguiar, E. Colegrove, T. Ablekim, S. K. Swain, K. G. Lynn, D. Kuciauskas, T. M. Barnes, and W. K. Metzger, "Interface characterization of single-crystal CdTe solar cells with VOC > 950 mV," IEEE J. Photovoltaics **6**(6), 1650–1653 (2016).

[6]E. Colegrove, B. Good, A. Abbas, H. Moutinho, S. Johnston, C.-S. Jiang, P. O'Keefe, J. M. Walls, D. S. Albin, and M. O. Reese, "Investigating the role of copper in arsenic doped Cd(Se,Te) photovoltaics," Sol. Energy Mater. Sol. Cells **246**, 111886 (2022).

[7]S. Rühle, "Tabulated values of the Shockley–Queisser limit for single junction solar cells," Sol. Energy **130**, 139–147 (2016).

[8]A. Shah, A. P. Nicholson, T. A. M. Fiducia, A. Abbas, R. Pandey, J. Liu, C. Grovenor, J. M. Walls, W. S. Sampath, and A. H. Munshi, "Understanding the copassivation effect of Cl and Se for CdTe grain boundaries," ACS Appl. Mater. Interfaces **13**(29), 35086–35096 (2021).

[9]S. C. Selvaraj, S. Gupta, D. Caliste, and P. Pochet, "Passivation mechanism in CdTe solar cells: The hybrid role of Se," Appl. Phys. Lett. **119**(6), 062105 (2021).

[10]T. A. M. Fiducia, B. G. Mendis, K. Li, C. R. M. Grovenor, A. H. Munshi, K. Barth, W. S. Sampath, L. D. Wright, A. Abbas, J. W. Bowers, and J. M. Walls, "Understanding the role of selenium in defect passivation for highly efficient selenium-alloyed cadmium telluride solar cells," Nat. Energy **4**(6), 504–511 (2019).

[11]R. Wang, M. Lan, and S.-H. Wei, "Enhanced performance of Se-alloyed CdTe solar cells: The role of se-segregation on the grain boundaries," J. Appl. Phys. **129**(2), 024501 (2021).

[12]A. Nagaoka, S. K. Swain, and A. H. Munshi, "Review on group-V doping in CdTe for photovoltaic application," IEEE J. Photovoltaics **14**(3), 397–413 (2024).

[13]P. Eyben, M. Xu, N. Duhayon, T. Clarysse, S. Callewaert, and W. Vandervorst, "Scanning spreading resistance microscopy and spectroscopy for routine and quantitative two-dimensional carrier profiling," J. Vac. Sci. Technol. B **20**(1), 471–478 (2002).

[14]P. Eyben, F. Clemente, K. Vanstreels, G. Pourtois, T. Clarysse, E. Duriau, T. Hantschel, K. Sankaran, J. Mody, W. Vandervorst, K. Mylvaganam, and L. Zhang, "Analysis and modeling of the high vacuum scanning spreading resistance microscopy nanocontact on silicon," J. Vac. Sci. Technol. B **28**(2), 401–406 (2010).

[15]L. Zhang, K. Ohuchi, K. Adachi, K. Ishimaru, M. Takayanagi, and A. Nishiyama, "High-resolution characterization of ultrashallow junctions by measuring in vacuum with scanning spreading resistance microscopy," Appl. Phys. Lett. **90**(19), 192103 (2007).

[16]C.-S. Jiang, R. Farshchi, T. Nagle, D. Lu, G. Xiong, L. M. Mansfield, and M. O. Reese, "Microelectronic structure and doping nonuniformity of phosphorus-doped CdSeTe solar cells," ACS Appl. Mater. Interfaces **17**(2), 3278–3288 (2025).

[17]Y. Chen, S. Farrell, G. Brill, P. Wijewarnasuriya, and N. Dhar, "Dislocation reduction in CdTe/Si by molecular beam epitaxy through in-situ annealing," J. Cryst. Growth **310**(24), 5303–5307 (2008).

[18]A. T. Mathew, H. Lott, E. Colegrove, M. R. Young, D. Kuciauskas, C. A. Wolden, and M. O. Reese, "Arsenic activation and compensation in single crystal CdTe bilayers," J. Appl. Phys. **137**(11), 115702 (2025).

[19]J. Frenkel, "On pre-breakdown phenomena in insulators and electronic semiconductors," Phys. Rev. **54**(8), 647–648 (1938).

[20]S. M. Sze, "Current transport and maximum dielectric strength of silicon nitride films," J. Appl. Phys. **38**(7), 2951–2956 (1967).

[21]Q. Long, S. A. Dinca, E. A. Schiff, M. Yu, and J. Theil, "Electron and hole drift mobility measurements on thin film CdTe solar cells," Appl. Phys. Lett. **105**(4), 042106 (2014).

[22]P. Ščajev, M. Nardone, C. Reich, R. Farshchi, K. McReynolds, D. Krasikov, and D. Kuciauskas, "As-doped polycrystalline CdSeTe: Localized defects, carrier mobility and lifetimes, and impact on high-efficiency solar cells," Adv. Energy Mater. **15**, 2403902 (2025).

[23]L. Wang, R. Nughays, X. Song, T. Bian, M. N. Hedhili, J. Yin, O. M. Bakr, and O. F. Mohammed, "Crystallographic orientation-dependent photo-response of planar cadmium telluride X-ray detectors," Cell Rep. Phys. Sci. **4**(12), 101723 (2023).

[24]Y. Jin and S. T. Dunham, "The impact of charged grain boundaries on CdTe solar cell: EBIC measurements not predictive of device performance," IEEE J. Photovoltaics **7**(1), 329–334 (2017).

[25]J. D. Poplawsky, C. Li, N. R. Paudel, W. Guo, Y. Yan, and S. J. Pennycook, "Nanoscale doping profiles within CdTe grain boundaries and at the CdS/CdTe interface revealed by atom probe tomography and STEM EBIC," Sol. Energy Mater. Sol. Cells **150**, 95–101 (2016).

[26]H. P. Yoon, P. M. Haney, D. Ruzmetov, H. Xu, M. S. Leite, B. H. Hamadani, A. A. Talin, and N. B. Zhitenev, "Local electrical characterization of cadmium telluride solar cells using low-energy electron beam," Sol. Energy Mater. Sol. Cells **117**, 499–504 (2013).